RESEARCH

Electronic and ring size effects of N-heterocyclic carbenes on the kinetics of ligand substitution reactions and DNA/protein interactions of their palladium(II) complexes
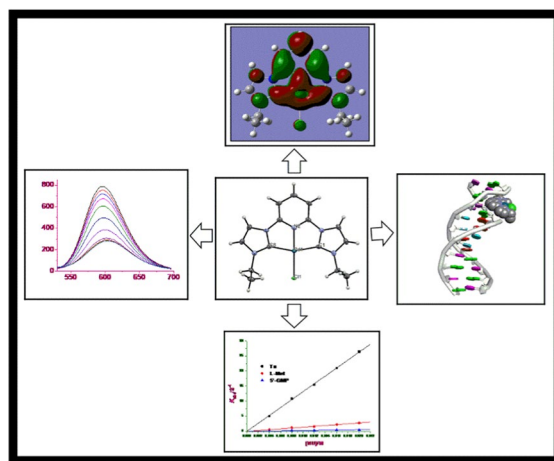
Reinner O. Omondi [ORCID] · **Deogratius Jaganyi** ·
Stephen O. Ojwach

Abstract The synthesis, substitution kinetics and DNA/BSA interactions of four cationic Pd(II) complexes [Pd(**1**)Cl]BF$_4$ (**Pd1**), [Pd(**2**)Cl]BF$_4$ (**Pd2**), [Pd(**3**)Cl]BF$_4$ (**Pd3**) and [Pd(**4**)Cl]BF$_4$ (**Pd4**), derived from the reaction of [PdCl$_2$(NCCH$_3$)$_2$] with ligands 2,6-bis(3-methylimidazolium-1-yl)pyridine dibromide (**1**), 2,6-bis(3-ethylimidazolium-1-yl)pyridine dibromide (**2**), 2,6-bis(1-methylimidazole-2-thione) pyridine (**3**), and 2,6-bis(1-ethylimidazole-2-thione) pyridine (**4**), respectively are reported. The complexes were characterised by various spectroscopic techniques and single crystal X-ray diffraction for compound **Pd2**. Kinetic reactivity of the complexes with the biologically relevant nucleophiles thiourea (**Tu**), L-methionine (**L-Met**) and guanosine 5′-monophosphate sodium salt (**5'-GMP**) was in the order: **Pd1 > Pd2 > Pd3 > Pd4**, which was largely dependent on the electronic and ring size of the chelate ligands, consistent with Density functional theory (DFT) simulations. The interactions of the complexes with calf thymus DNA (CT-DNA) and bovine serum albumin (BSA) binding titrations showed strong binding. Both the experimental and in silico data reveal CT-DNA intercalative binding mode.

Graphical abstract

R. O. Omondi · S. O. Ojwach (✉)
School of Chemistry and Physics, University of KwaZulu-Natal, Scottsville, Private Bag X01, Pietermaritzburg 3209, South Africa
e-mail: Ojwach@ukzn.ac.za

D. Jaganyi
School of Pure and Applied Sciences, Mount Kenya University, P.O. Box 342-01000, Thika, Kenya

D. Jaganyi
Department of Chemistry, Faculty of Applied Sciences, Durban University of Technology, P.O. Box 1334, Durban 4000, South Africa

Introduction

N-heterocyclic carbenes (NHCs; CNC) and their derivatives (NHEs; ENE, where E = S, Se and Te) are versatile ligands used in the coordination chemistry of transition metals (Wang and Robinson 2011; Jia et al. 2009; Manjare et al. 2012; Collado-Martinez et al. 2016; Onar et al. 2019; Hussaini et al. 2019; Kumar et al. 2017; Ostrowska et al. 2021). The attractive features of their transition metal complexes have resulted to their wide range of applications in material science (Han et al. 2014; Zhang et al. 2015), catalysis (Ghavale et al. 2015; Jia et al. 2020) and therapeutics (Han et al. 2014; Hindi et al. 2009; Seliman et al. 2017; Jomaa et al. 2018). The NHCs and NHEs ligands are often used to stabilise organometallic centres, owing to their fascinating chemical properties such as strong σ-donating and poor (weak or even negligible) π-accepting abilities, saturation or aromaticity, forming complexes that are resistant to thermal decomposition (Manjare et al. 2012; Jia et al. 2015, 2020; Miecznikowski et al. 2012). The stronger σ-donor properties of NHEs in comparison to both NHC and phosphine is attributable to the presence of a larger contribution (66%) of the zwitterionic form (NHC$^+$–E$^-$) (Rani et al. 2017).

Metal-NHCs have demonstrated promising biological results (stemming from their favourable biocompatibility and molecular targeting properties), and among them Pd- NHC complexes have gain significant traction over the last decade (Bernd et al. 2020; Lee et al. 2015; Akkoç et al. 2017; Ghdhayeb et al. 2017). Pd-NHC compounds demonstrate appreciable stability under physiological conditions, which enhances their delivery to tumour tissues and thus minimising toxic side effects. Apart from their acceptable delivery method, Pd(II)-NHC complexes exhibit good solubility in the aqueous media (Al Nasr et al. 2020).

Che and the group (Fong et al. 2016) have reported the antitumour activity of a class of palladacyclic complexes supported by NHCs ligands. The results of the study revealed that the complexes are more active than palladacyclic derivatives with no NHCs ligands (i.e., with weaker σ-donors). The complexes also demonstrated high stability under physiological conditions. In addition, the authors found Pd(II)-NHCs to display better in vitro cytotoxicity than cisplatin in all the tested cancer lines. In a previous study, Gosh and co-workers (Ray et al. 2007), examined the antiproliferative properties of Pd(II)-NHC complexes. The compounds were found to have remarkable activity on MCF-7, HCT-116 and HeLa with better IC$_{50}$ values than those of cisplatin. Noteworthy, most investigations have demonstrated that the main target for Pd-NHEs in cancer cells is DNA similar to cisplatin's (Ray et al. 2007; Teyssot et al. 2009), with three distinct modes of interactions i.e., groove binding, intercalative, and electrostatic. These results encouraged us to consider Pd(II) complexes anchored on functionalised NHC and NHEs ligands. The substitution kinetics of the complexes with biological nucleophiles; thiourea (**Tu**), L-methionine (**L-Met**) and guanosine-5'-monophosphate (**5'-GMP**) are hereby reported. We also explored the interactions of the complexes with the DNA and BSA protein and their molecular docking studies.

Experimental section

Syntheses of palladium metal complexes

*[{2,6-bis(3-methylimidazolium-1-yl)pyridine dibromide}PdCl]BF$_4$ (**Pd1**)* To a solution of ligand 2,6-bis(3-methylimidazolium-1-yl)pyridine dibromide, **1** (0.50 g, 1.25 mmol) in CH$_3$CN (30 mL) was added Ag$_2$O (0.29 g, 1.25 mmol) and the reaction was stirred at 50 °C for 24 h. To the mixture, AgBF$_4$ (0.24 g, 1.26 mmol) was added, followed by PdCl$_2$(MeCN)$_2$ (0.32 g, 1.25 mmol) in a dark-room environment with stirring at 50 °C for 24 h. After the reaction period, the mixture was cooled to room temperature and filtered. The filtrate was then evaporated in *vacuo* and the yellow residue washed with CH$_2$Cl$_2$ and diethyl ether to obtain compound **Pd1** as a brown-yellow solid. Yield: 0.42 g (72%). ^{1}H NMR (400 MHz, DMSO-d$_6$): δ$_H$ (ppm): 3.91 (s, 6H, CH$_3$); 7.61 (s, 2H, imid); 7.92 (d, $^3J_{HH}$ = 8.2, 2H, py); 8.35 (s, 2H, imid); 8.51 (t, $^3J_{HH}$ = 8.2, 1H, py). ^{13}C NMR (DMSO-d$_6$): δ$_C$ (ppm): 36.51 (CH$_3$); 108.69 (imidazole, CH); 117.93 (pyridine, CH); 125.34 (imidazole, CH); 146.47 (pyridine, CH); 150.25 (pyridine, CH); 166.35 (pyridine, C). FT-IR (cm^{-1}): υ(C–H, aromatic) = 3615; υ(C–H, alkyl) = 3132; υ(C=N, imidazole) = 1619; υ(C=N, pyridine) = 1587; υ(C-N, imidazole) = 1033. LC MS/ESI$^+$, *m/z* (%) = 382 (100% [M-BF4]$^+$). Anal. Calcd (%) for C$_{13}$H$_{15}$BClF$_4$N$_5$Pd:

C, 33.22; H, 3.22; N, 14.90%. Found: C, 33.51; H, 2.98; N, 14.74%.

*[{2,6-bis(3-ethylimidazolium-1-yl)pyridine dibromide}PdCl]BF$_4$ (**Pd2**)* Complex **Pd2** was synthesised in a similar fashion using ligand 2,6-bis(3-ethylimidazolium-1-yl)pyridine dibromide, **2** (0.53 g, 1.25 mmol), Ag$_2$O (0.29 g, 1.25 mmol), AgBF$_4$ (0.24 g, 1.26 mmol), and PdCl$_2$(MeCN)$_2$ (0.32 g, 1.25 mmol) to afford a brown-yellow solid. Further recrystallization in CH$_2$Cl$_2$/Et$_2$O solution led to the formation of single-crystals suitable for X-ray crystallography analysis. Yield: 0.46 g (74%). ^{1}H NMR (400 MHz, DMSO-d6): δ_H (ppm): 1.37 (t, $^3J_{HH}$=7.2, 6H, CH$_3$); 4.41 (dd, $^3J_{HH}$=7.2, 4H, CH$_2$); 7.75 (d, $^3J_{HH}$=2.1, 2H, imidazole, CH); 7.94 (d, $^3J_{HH}$=8.2, 2H, imidazole, CH); 8.38 (d, $^3J_{HH}$=2.1, 2H, pyridine, CH); 8.52 (t, $^3J_{HH}$=8.2, 1H, pyridine, CH). ^{13}C NMR (DMSO-d$_6$): δ_C (ppm): 16.14 (CH$_3$); 44.43 (CH$_2$); 108.73 (imidazole, CH); 118.22 (pyridine, CH); 123.67 (imidazole, CH); 146.46 (pyridine, CH); 150.34 (pyridine, CH); 165.88 (pyridine, C). FT-IR (cm^{-1}): υ(C–H, aromatic)=3138; υ(C–H, alkyl)=2989; υ(C=N, imidazole)=1619; υ(C=N, pyridine)=1491; υ(C-N, imidazole)=1035. LC MS/ESI$^+$, *m/z* (%)=410 (100% [M-BF4]$^+$). Anal. Calcd (%) for C$_{15}$H$_{19}$BClF$_4$N$_5$Pd: C, 36.18, H, 3.85; N, 14.06. Found: C 35.81; H, 3.53, N, 14.34%.

*[{2,6-bis(3-methylimidazole-2-thione)pyridine}PdCl]BF$_4$ (**Pd3**)* This compound was prepared by introducing a mixture of ligand 2,6-bis(1-methylimidazole-2-thione)pyridine, **3** (0.12 g, 0.39 mmol) and NaBF$_4$ (0.04 g, 0.39 mmol) in CH$_2$Cl$_2$ (10 mL) to a solution of [PdCl$_2$(NCMe)]$_2$ (0.10 g, 0.39 mmol) in CH$_2$Cl$_2$ (20 mL). The resultant mixture was then stirred at room temperature for 12 h and filtered to afford complex **Pd3** as an analytically pure compound. Yield: 0.14 g (67%). ^{1}H NMR (400 MHz, DMSO-d$_6$): δ_H (ppm): 3.80 (s, 6H, CH$_3$); 7.85 (d, $^3J_{HH}$=2.4, 2H, imidazole, CH); 8.10 (d, $^3J_{HH}$=8.2, 2H, imidazole, CH); 8.21 (d, $^3J_{HH}$=2.4, 2H, pyridine, CH); 8.67 (t, $^3J_{HH}$=8.2, 1H, pyridine, CH). ^{13}C NMR (DMSO-d$_6$): δ_C (ppm): 35.71 (CH$_3$), 116.80 (imidazole, CH), 117.53 (imidazole, CH), 120.12 (imidazole, CH), 140.17 (pyridine CH), 162.2 (pyridine, C), 170.53 (C=S). FT-IR (cm^{-1}): υ(C–H, aromatic)=3489; υ(C–H, alkyl)=3102; υ(C=N, imidazole)=1603 υ(C=N, pyridine)=1473; υ(C=S, imidazole)=1240, υ(C-N, imidazole)=1019. LC MS/ESI$^+$, *m/z* (%)=489 (8% [(M-BF$_4$)+2Na]$^+$).

Anal. Calcd (%) for C$_{13}$H$_{13}$BClF$_4$N$_5$PdS$_2$: C, 29.35; H, 2.46; N, 13.16; S, 12.05%. Found: C, 29.02; H, 2.17; 12.79, S, 12.26%.

*[{2,6-bis(3-ethylimidazole-2-thione)pyridine} PdCl]BF$_4$ (**Pd4**)* The procedure used in the preparation of **Pd3** was employed in the synthesis of **Pd4**, using ligand 2,6-bis(1-ethylimidazole-2-thione)pyridine, **4** (0.13 g, 0.39 mmol), PdCl$_2$(NCMe)$_2$ (0.10 g, 0.39 mmol), and NaBF$_4$ (0.04 g, 0.39 mmol). Yellow solid. Yield: 0.15 g (69%). ^{1}H NMR (400 MHz, DMSO-d$_6$): δ_H (ppm): 1.44 (t, $^3J_{HH}$=7.3, 6H, CH$_3$); 4.23 (dd, $^3J_{HH}$=7.2, 4H, CH$_2$); 7.97 (d, $^3J_{HH}$=2.4, 2H, imidazole, CH); 8.13 (d, $^3J_{HH}$=8.2, 2H, imidazole, CH); 8.25 (d, $^3J_{HH}$=2.4, 2H, pyridine, CH); 8.69 (t, $^3J_{HH}$=8.2, 1H, pyridine, CH). ^{13}C NMR (DMSO-d$_6$): δ_C (ppm): 13.80 (CH$_3$), 44.54 (CH$_2$), 116.72 (pyridine, CH), 117.55 (imidazole, CH), 120.81 (imidazole, CH), 140.12 (pyridine, CH), 164.66 (pyridine, C), 170.45 (C=S). FT-IR (cm^{-1}): υ(C–H, aromatic)=3546; υ(C–H, alkyl)=3092; υ(C=N, imidazole)=1600; υ(C=N, pyridine)=1458; υ(C=S)=1153; υ(C-N, imidazole)=1021. LC MS/ESI$^+$, *m/z* (%)=474 (55% [M-BF4]$^+$). Anal. Calcd (%) for C$_{15}$H$_{17}$BClF$_4$N$_5$PdS$_2$: C, 32.16; H, 3.06; N, 12.50; S, 11.45%. Found: C, 32.44; H, 3.23; N, 12.15; S, 11.76%.

Results and discussion

Syntheses and structural characterisation of Pd(II) complexes

The preparation of ligands **1** and **2** was carried out by employing the previously described method (Chen and Lin 2000), through the reaction of 2,6-dibromopyridine with the corresponding imidazoles under solvent free conditions at 150 °C (Scheme 1). In contrast, ligands **3** and **4** were prepared according to the well-established synthetic procedure (Jia et al. 2015), via the condensation reactions of pyridine bridged imidazolium dibromide derivatives with sulfur powder in the presence of K$_2$CO$_3$ (Scheme 1) and were isolated in moderate yields. Detailed synthetic protocols, their spectroscopic and analytical data are given in the supplementary section. The dicarbene Pd(II) complexes **Pd1** and **Pd2**, were obtained in the sequential one-pot reaction of PdCl$_2$(NCMe)$_2$, Ag$_2$O, AgBF$_4$ with the respective
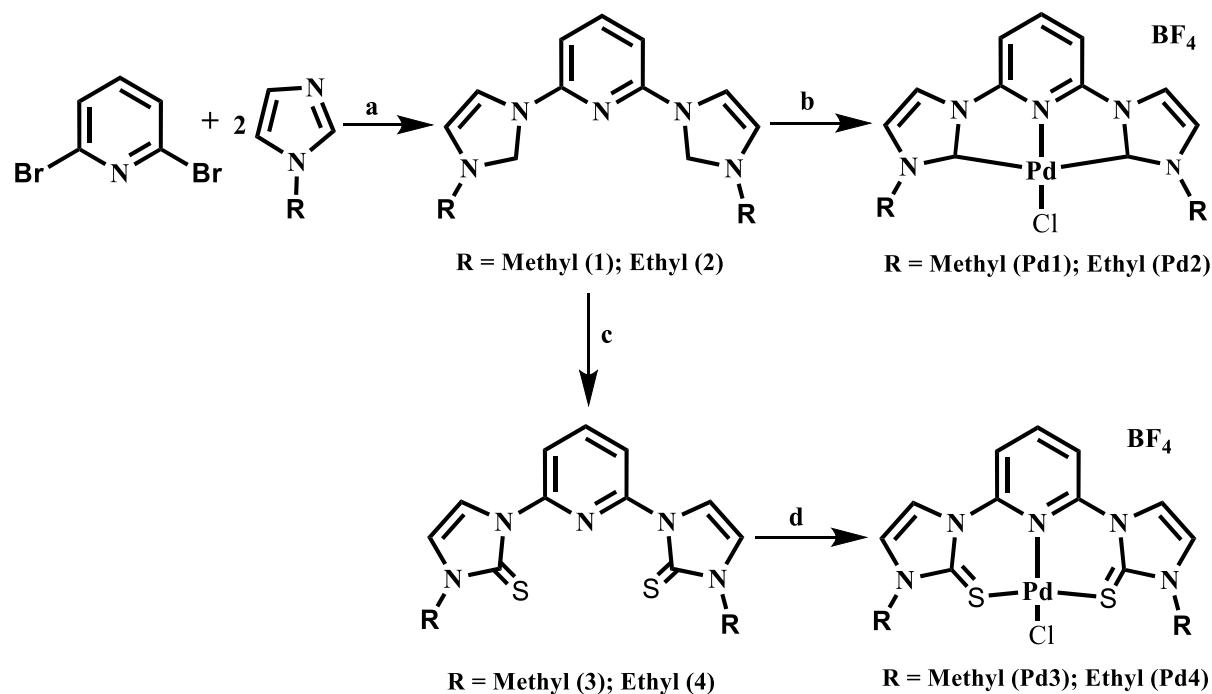
Scheme 1 Synthetic pathways map for the ligands and their respective Pd(II) complexes. *Reagents and conditions*; **a** neat conditions, 150 °C, 20 h; **b** Ag$_2$O, PdCl$_2$(NCMe)$_2$, AgBF$_4$, MeCN, 50 °C; **c** S$_8$ powder, K$_2$CO$_3$, MeOH, 8 h; **d** PdCl$_2$(NCCH$_3$)$_2$, NaBF$_4$, CH$_2$Cl$_2$, room temperature, 12 h

ligands **1** and **2** in MeCN at 50 °C as described in Scheme 1. On the contrary, the reactions of **3** and **4** with equimolar amounts of [PdCl$_2$(NCMe)$_2$] in the presence of NaBF$_4$ in CH$_2$Cl$_2$ produced the corresponding complexes **Pd3** and **Pd4** (Scheme 1).

The formation and identities of the complexes were confirmed by ^{1}H, ^{13}C NMR (Figs. S1-S16) and FT-IR (**Figs. S17–S25**) spectroscopies, mass spectrometry (Figs. S26–S32), elemental analyses, and single crystal X-ray analyses (for **Pd2**). For instance, the ^{1}H NMR spectrum of free ligand **1** displayed a singlet peak at δ 10.63 ppm, ascribed to the imidazolium CH proton and upon complexation to form complex **Pd1**, the peak disappeared (Fig. S9), indicative of the coordination of the CH moiety to the Pd(II) atom. Likewise, from ^{13}C NMR spectra, the downfield shifts of the carbene carbon at 145.20 ppm (**1**) to 166.35 pm (**Pd1**) is consistent with the formation of the complex (Fig. S16). Similarly, the successful coordination of the ligands to produce the corresponding Pd(II) complexes was determined from their respective FT-IR spectra. For instance, a shift of the absorption bands at 1605 cm^{-1} (C=N, imidazole) and

1531 cm^{-1} (C=N, pyridine) in **1** to higher frequency values of 1619 and 1587 cm^{-1} in **Pd1** respectively (Fig. S25) affirmed the coordination of the Pd(II) ion to the nitrogen atom of pyridine and the carbene in the imidazolium unit. Positive electron ionisation mass spectrometry (ESI-LC–MS) further proved the formation of the Pd-complexes. For example, the LC–MS spectrum for **Pd1** gave characteristic peak at *m/z* at 382 (**Fig**. S29a) corresponding to its exact mass of 382.01. In addition, the experimental isotopic mass distribution patterns were in congruous with the calculated isotopic mass distributions (**Fig**. **S29b**). Elemental analyses data for all the complexes showed close agreement with the theoretical calculations validating the proposed structures and their purity.

X-ray diffraction analysis

Single crystals suitable for crystallographic analyses of complex **Pd2** were obtained by slow diffusion of diethyl ether/acetonitrile layered solutions. The molecular structure of complex **Pd2** is shown in

Fig. 1, while the crystallographic data and structural refinement parameters are summarised **in Table S1.**

　　Complex **Pd2** crystallised in the monoclinic space group, P 21/n. The molecular structure reveals one tridentate ligand unit and Cl atom to give a nominally square planar geometry. The dihedral angles N(2)–Pd(1)–C(1) of 79.46(12)° and N(2)–Pd(1)–C(8) of 79.03(13)° deviate considerably from the expected 90° for a perfect square planar geometry. Similarly, the bite angles C(1)–Pd(1)–C(8) of 158.50(14)° depart significantly from 180°, consistent with a distorted square planar geometry. Therefore, the geometry around the Pd(II) ion could be described as *pseudo* square planar (Yang et al. 2007). The average bond distance Pd–C$_{av}$ (2.033 Å) is within the range 1.996 ± 0.038 Å averaged for 15 related Pd structures (Groom et al. 2016). The bond length Pd(1)–Cl(1) 2.303(8) Å compares reasonably well with the mean distance of 2.365 ± 0.022 Å calculated from 14 related structures (Cooper 2020).

DFT calculations

For an in depth understanding of the structural properties of the complexes, quantum chemical calculations
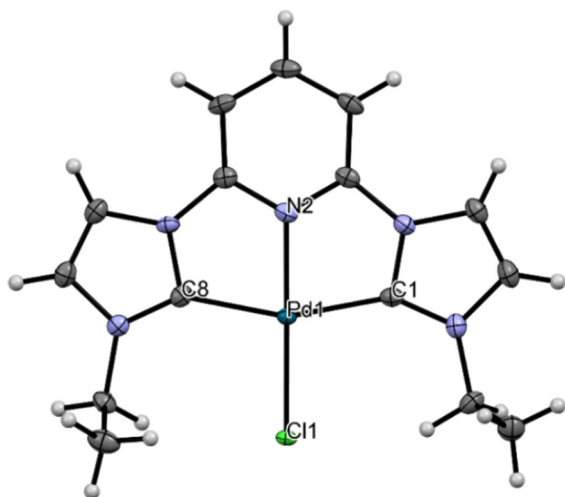

Fig. 1 Molecular structure of **Pd2**, depicting the coordination environment of Pd(II) centre. The hydrogen atoms are shown as spheres of common arbitrary radius. Selected bond lengths [Å]: Pd(1)–N(2), 1.966(3); Pd(1)–C(1), 2.032(3); Pd(1)–C(8), 2.035(3); Pd(1)–Cl(1), 2.3033(8). Selected bond angles [°]: N(2)–Pd(1)-C(1), 79.46(12); N(2)–Pd(1)–C(8), 79.03(13); C(1)–Pd(1)–C(8), 158.50(14); N(2)–Pd(1)–Cl(1), 179.15(9); C(1)–Pd(1)–Cl(1), 100.91(10); C(8)–Pd(1)–Cl(1), 100.59(10)

were performed. The modelled geometry structures, frontier orbital density distributions (HOMOs and LUMOs), and planarity of the complexes are given in Fig. S33, while a summary of the selected geometrical data are provided in Table S2. Both the HOMO and LUMO orbitals of complexes **Pd1** and **Pd2** reveal that the electron density is centred primarily on the Pd(II) metal ions, chelating ligands, and partially on the chlorido ligands. On the other hand, the HOMOs and LUMOs of compounds **Pd3** and **Pd4** are significantly concentrated on the metal centres, imidazolyl units and the chlorido atoms. Notably, the significant distribution of the LUMOs on the Pd-metal centre, indicate the potential σ-donor ability of the chelating ligand. The formation of a more electron rich Pd(II) metal centre stabilises the ground state, while destabilising the five-coordinate transition state. Moreover, the chemical reactivity of the complexes is related to the $\Delta E_{LUMO–HOMO}$ energy gap, where compounds with smaller gaps were more reactive than those with large gaps. The optimized geometries of the complexes reveal that **Pd3** and **Pd4** suffer distortion to accommodate steric repulsions, causing the twisting of the chelating ligands and hence loss of planarity.

Solution stability studies

The stability of complexes **Pd1–Pd4** under *pseudo* physiological conditions (50 µM Tris buffer containing 50 mM NaCl, pH 7.2) were assessed by time-dependent UV–Vis absorption spectroscopy. It has been shown that the interactions of the metal-complexes with water molecules influence their rates of substitution kinetics and resultant bio-activity (Zhao et al. 2017). As observed in Fig. S34, the UV–Vis spectra of the complexes showed no significant changes in MLCT absorption bands (both in intensity and position), ascribable to their non-interaction with H$_2$O molecules. Thus, the compounds displayed sufficient stability in the aqueous solution for at least 72 h.
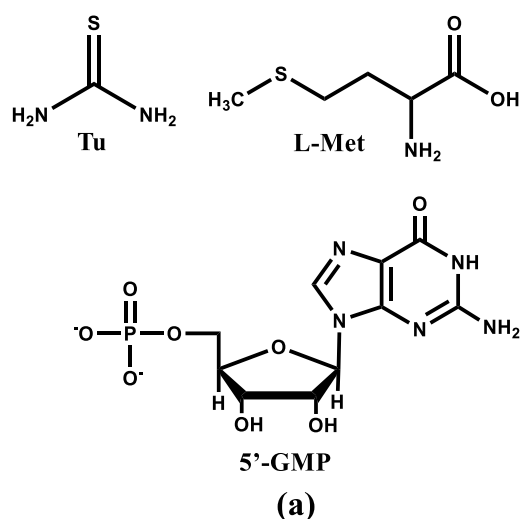
Electrochemical studies

Redox properties of the complexes were studied by cyclic voltammetry (CV) under N$_2$, with potential range of − 2.0 to 2.0 V. Scan rate dependency of the CVs of the complexes are indicated in **Fig. S35**. The cyclic voltammograms of the complexes are

suggestive of irreversible reductive processes (consisting of two electron transfer) occurring at –1.2, – 1.4, –0.9, and –1.0 V for **Pd1**–**Pd4**, respectively. The irreversible cathodic waves of the complexes were associated with the reduction of Pd(II)/(0), assigned to the sigma-donor nature of ligand scaffold, towards the metal centre (Shabbir et al. 2016). This is also supported by the relatively higher HOMOs energy for the complexes with ethyl substituents (**Pd2** and **Pd4**) than those methyl groups (**Pd1** and **Pd3**).

Kinetic and mechanistic study

Concentration effect

The reactivity of the complexes towards biological nucleophiles (i.e., **Tu**, **L-Met**, and **5'-GMP**, Fig. 2) were evaluated spectrophotometrically at physiological conditions. Typical kinetic trace recorded from stopped-flow spectrophotometer for the reaction of **Pd1** with **Tu** is shown in Fig. 2. All the kinetic profiles fitted well on a single-exponential decay function to generate the observed *pseudo*-first-order rate constants (k_{obs}) using equation (S1), signifying that the reactions were first-order. The k_{obs} values obtained were plotted against nucleophiles concentration [Nu]. Representative plots of k_{obs} against [Nu] obtained for **Pd1** at 298 K is presented in Fig. 2b, while the spectra of complexes **Pd2**-**Pd4** are displayed in Fig. S36. A linear dependence of k_{obs} on [Nu] with zero intercept was observed in all the plots, indicative of irreversible or non-solvotic pathways (Bellam et al. 2019). The second-order rate constants (k_2) were obtained from the dependence of k_{obs} on [Nu] using equation (S2), and the values are provided in Table 1. The relationship between k_{obs} and [Nu] can best be illustrated by equation (S3).

From the second-order rate constants values, k_2, provided in Table 1, the reactivity of the Pd(II) complexes increases marginally by factors ranging from 1.3 to 1.6. The trend of the reactivity of the complexes decreases following the order; **Pd1** > **Pd2** > **Pd3** > **Pd4**. The observed reactivity trend can be ascribed to both electronic and steric contributions of the spectator ligand(s). Notably, the lower reactivities of complexes **Pd2** & **Pd4** in relation to complexes **Pd1** and **Pd3** respectively is attributed to the superior σ-donation capability of the ethyl substituents (**Pd2** and **Pd4**) than the methyl groups in **Pd1** and **Pd3**. The net effect is the accumulation of electron density on the Pd metal centre, which hinders the incoming nucleophiles through electron–electron repulsions. The reasoning is consistent with the raised E_{HOMO} of **Pd2** in comparison to **Pd1** (Table S2). This is also reflected
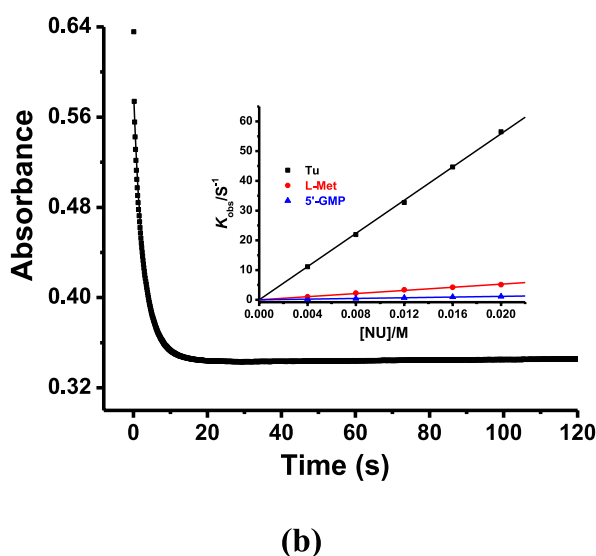

Fig. 2 **a** Chemical structures for the entering ligands. **b** Time resolved stopped-flow kinetic trace at 345 nm of **Pd1**, at T = 298 K, 50 μM Tris–HCl buffer (pH = 7.2), and 50 mM NaCl {Inset: plot of k_{obs} vs [Nu]}

Table 1 Second order rate constants, k_2, and activation parameters for the substitution reactions of **Pd1**–**Pd4** with **Tu**, **L-met** and **5'-GMP** at pH = 7.2 (50 µM Tris–HCl buffer and 50 mM NaCl)

Complex	Nu	k_2/M^{-1} s^{-1}	$\Delta H^{\neq}$/ kJ mol^{-1}	$-\Delta S^{\neq}$/Jmol^{-1} K^{-1}	$\Delta G^{\neq}_{25\,°C}$/kJ mol^{-1}
Pd1	**Tu**	2791 ± 19	14 ± 1	132 ± 4	53 ± 3
	L-Met	263 ± 5	18 ± 1	137 ± 3	59 ± 2
	5'-GMP	58 ± 1	26 ± 1	124 ± 4	63 ± 3
Pd2	**Tu**	2122 ± 13	15 ± 1	131 ± 3	54 ± 2
	L-Met	204 ± 4	21 ± 1	132 ± 4	60 ± 3
	5'-GMP	44 ± 2	26 ± 1	125 ± 3	63 ± 2
Pd3	**Tu**	1315 ± 9	28 ± 1	90 ± 3	55 ± 2
	L-Met	139 ± 3	41 ± 1	66 ± 3	61 ± 2
	5'-GMP	27 ± 2	44 ± 1	70 ± 3	65 ± 2
Pd4	**Tu**	930 ± 7	29 ± 2	89 ± 5	56 ± 4
	L-Met	108 ± 4	40 ± 1	71 ± 3	61 ± 2
	5'-GMP	22 ± 2	44 ± 1	71 ± 3	65 ± 2

by the positive NBO charges of Pd(II) ions which decrease from 0.276 (**Pd1**) to 0.262 (**Pd2**) as shown in **Table S2.**

The argument is well validated by the raised E_{HOMO} values which are ordered as; **Pd3** $(-6.6734$ eV$) <$ **Pd4** $(-6.6007$ eV$)$, Table 2. The observed higher reactivity of C^N^C (**Pd1** and **Pd2**) in comparison to the S^N^S analogues **Pd3** and **Pd4** could also be due to the rigid five-membered ring and planarity in complexes **Pd1** and **Pd2** (**Fig. S33**). The smaller dihedral angles for N-Pd–C of 79.252° and 79.281° for **Pd1** and **Pd2** respectively (**Table S2**), result in strained chelate framework, consistent with enhanced intrinsic reactivities. In contrast, the structures of **Pd3** and **Pd4** are twisted out of the mean plane (**Fig. S33**), at dihedral angles, for instance N-Pd-S of 88.812 ° (**Pd3**) and 88.565 ° (**Pd4**) (**Table S2**). The boat-shaped conformation of **Pd3** and **Pd4** introduces steric effects and thereby impeding nucleophilic attack. In addition, the analysis of the of NBO charges on the Pd(II) depicts fairly unusual negative values of -0.053 for **Pd3** and -0.061 for **Pd4**, tenably due to the fact that S-atom is

more polarisable than C-atom. Notably, the S-atom is larger and have more loosely held electrons than the C-atom, and thus is more willing to share the electron density with the Pd(II) ion through the σ-framework (Matta, Gillespie 2002).

The trend in the nucleophilicity of the entering ligands decreases in the form **Tu > L-Met > 5'-GMP** (Table 1), highlighting that the reactivity is controlled by both electronic and steric effects. Sulfur entering ligands (**Tu** and **L-Met**) show higher lability than the nitrogen entering ligand (**5'-GMP**). The observation is attributable to the soft-acid nature of Pd(II), which has a higher attraction for sulfur compounds (soft bases) (Jovanović et al. 2016). The entering ligand, **Tu** exhibit the highest reactivity because it combines the properties of the thioethers (function as σ-donors and π-acceptors), and thiolates (acts as π-donors) (Murray and Hartley 1981). In addition, the two amine groups in **Tu** in relation to **L-Met** improves the nucleophilicity on the S-atom as opposed to the methyl substituent. The bulkiness of **5'-GMP** hinders it from competing with **Tu** (least sterically demanding) and **L-Met** (moderate steric demands).

Table 2 DNA binding constants and number of binding sites for Pd(II) complexes

Complex	UV–Vis titration		EB fluorescence quenching titration				
	K_b (10^5 M^{-1})	ΔG/k J mol^{-1}	K_{sv} (10^4 M^{-1})	K_{app} (10^9 M^{-1})	k_q (10^{12} M^{-1} s^{-1})	K_F (10^5 M^{-1})	n
Pd1	31.24 ± 0.81	-37.05	7.79 ± 0.55	2.00 ± 0.23	3.39 ± 0.19	2.26 ± 0.17	1.13
Pd2	2.30 ± 0.11	-30.59	6.70 ± 0.39	1.68 ± 0.26	2.91 ± 0.19	1.20 ± 0.14	1.10
Pd3	2.12 ± 0.13	-30.39	4.80 ± 0.20	1.56 ± 0.08	2.08 ± 0.21	0.89 ± 0.06	0.79
Pd4	1.54 ± 0.13	-29.60	0.63 ± 0.04	0.30 ± 0.05	0.28 ± 0.01	0.10 ± 0.03	0.81

Temperature effect and iso-kinetic relationship

To ascertain the mechanism of the substitution process followed by the complexes, the reaction temperatures were varied from 298 to 318 K. The enthalpy of activation ($\Delta H^{\neq}$), entropy of activation ($\Delta S^{\neq}$) were computed from equation (S4). Gibbs free energy of activation ($\Delta G^{\neq}_{25\,°C}$) was derived from equation (S5). Representative plots obtained for **Pd1** are given in Fig. 3a (plots for **Pd2**-**Pd4** are shown in Fig. S37). The calculated values of thermal parameters are depicted in Table 1. The higher reactivity of **Pd1** and **Pd2** in relation to **Pd3** and **Pd4** is attributed to the small values of $\Delta H^{\neq}$ (Table 1), signifying low energy barrier that is associated with the process of the formation of bonds in the transition state. The small positive values $\Delta H^{\neq}$ and the large negative values $\Delta S^{\#}$ (Table 1) indicate an associative mechanism, where Pd-Cl bond breakage and Pd-nucleophile bonds formation are concerted (Atwood 1997). The large sensitivity of the second order rate constants to the nucleophiles is consistent with an associative mode of ligand substitution reaction (Petrović et al. 2012). The magnitude of $\Delta G^{\neq}_{25\,°C}$ (obtained from Eq. 5) for the reactions of complexes **Pd1**–**Pd4** with the three biological nucleophiles are all comparable, indicating that the reactions follow a similar associative mechanism (Bellam et al. 2019, 2018).
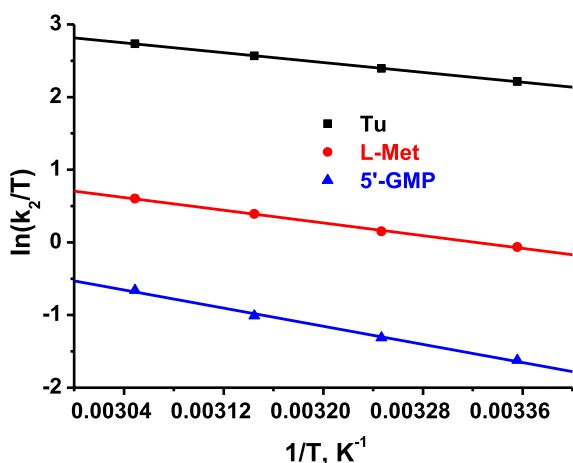
Linear plots of $\Delta H^{\neq}$ and $\Delta S^{\#}$ for the kinetic reactions displayed the existence of a linear free energy relationship (LFER) between the two thermal parameters (Fig. 3b). The *iso*-kinetic temperatures and Gibbs free energies ($\Delta G^{\neq}$) were respectively determined from the slopes and intercepts of the plots. The *iso*-kinetic temperature and $\Delta G^{\neq}$ were predicted at 387.03 K, and at 66,464.54 kJ mol^{-1}, respectively. Similarly, LFER/isokinetic plots illustrate that the kinetic reactivity of the complexes followed the same associative mechanism (Bellam et al. 2019, 2018).

CT-DNA interactions studies

UV–Vis absorption spectral studies

Electronic absorption spectroscopy studies were performed to determine the mode and extent of binding of the complexes to CT-DNA. Typical absorption spectral titration curves of complex **Pd1** in the absence and presence of DNA, at varying concentration are shown in Fig. 4, while the spectra for compounds **Pd2**–**Pd4** are given in **Fig. S38**. The spectra of these complexes displayed well-resolved bands in the range 250–300 nm, arising from the intra-ligand $\pi \rightarrow \pi^*$ charge transfer transitions (Sathyadevi et al. 2011).

Upon the addition of CT-DNA, the bands of complexes **Pd1**–**Pd4** demonstrated significant
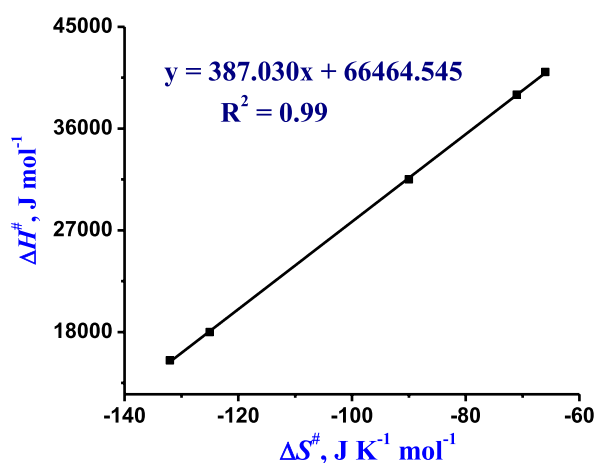
Fig. 3 **A)** Plots for the reaction of **Pd1** with the nucleophiles at pH = 7.2 (50 μM Tris–HCl buffer and 50 mM NaCl) and temperature range of 298–318 K. **b** *Iso*-kinetic plots for **Pd1**-**Pd4** with the biological nucleophiles
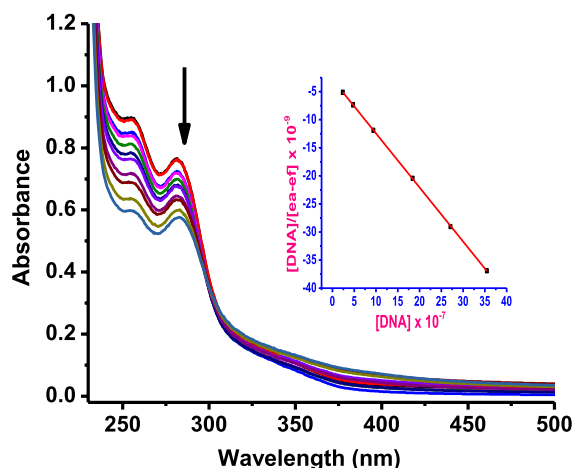
Fig. 4 Absorption spectral changes of **Pd1** [20 µM] in Tris buffer solution at pH = 7.2, with the successive addition of CT-DNA [0–80 µM], at room temperature. The arrow indicates absorbance changes with the increasing CT-DNA concentration. Inset: plot of [CT-DNA] versus $[DNA]/(\varepsilon_a - \varepsilon_f)$

reduction in the absorption bands (hypochromism of ~ 5–35%), demonstrating the existence of intercalative mode of binding (Balakrishnan et al. 2019). Of note such spectral changes are usually observed upon binding to guanine N_7 atom (Protas et al. 2018). The extent and strength of intrinsic binding constants (K_b) of the complexes to CT-DNA were determined from Wolfe-Shimer equation (S6) and the results are provided in Table 2. The K_b values of $(31.24 \pm 0.81) \times 10^5$ (**Pd1**), $(2.30 \pm 0.11) \times 10^5$ (**Pd2**), $(2.12 \pm 0.13) \times 10^5$ (**Pd3**), and $(1.54 \pm 0.13) \times 10^5$ M^{-1} (**Pd4**), compare well with related Pd(II) complexes obtained in literature (Franich et al. 2019; Karami et al. 2019; Mitra et al. 2018). Noteworthy, intercalative binding mode is largely sensitive to planarity of the chelating ligand(s) available for stacking, thus explaining the lower binding affinity for **Pd3** and **Pd4** (which suffer from distortion due to ring strain as depicted in the DFT Fig. S33). The free energy (ΔG) of the complex-DNA adduct was evaluated using van't Hoff equation (S7), and the results are presented in Table 2. The calculated negative ΔG values of **Pd1**–**Pd4** highlight the energetically favourable and spontaneity of the Pd(II) complexes towards CT-DNA (Mukherjee et al. 2017; Karami et al. 2018).

Competitive fluorescence measurements for CT-DNA

With the aim to further confirm the mode of binding between CT-DNA and complexes **Pd1**–**Pd4**, fluorescent-quenching assay based on the EB displacement from EB-DNA adduct was performed. Changes in the fluorescence spectra of EB-DNA composite in the absence and presence of varying concentration of the complexes is indicated in Fig. 5 for **Pd1** and Figs. S39–S41 for **Pd2**–**Pd4**, respectively. The incremental additions of complexes **Pd1**–**Pd4** to EB-CT-DNA system caused appreciable decrease in the fluorescence intensity (35–45%), suggestive of the complexes binding abilities to the DNA (Tarushi et al. 2013; Koumousi et al. 2012). The Stern–Volmer quenching constant (K_{sv}) and bimolecular quenching rate constant (k_q), were calculated from the Stern–Volmer equation (S8), and the data are given in Table 2. The K_{sv} values of **Pd1**–**Pd4** (magnitude 10^3–10^4 M^{-1}), signifying that the studied complexes can displace bound EB from the CT-DNA via intercalative mode (Table 2) (Wei et al. 2020). The values of apparent binding constant (K_{app}) obtained from equation (S9) are presented in Table 2. The calculated K_{app} values (magnitude 10^8- 10^9 M^{-1}) are higher than the values for classical intercalators binding constant (10^7 M^{-1}) (Cory et al. 1985), confirming a strong intercalative interaction mode. The K_q values for the Pd-complexes found in the magnitude (10^{11}–10^{12} M^{-1} s^{-1}), are greater than most known dynamic fluorescent biopolymers (10^{10} M^{-1} s^{-1}), indicating a static quenching mechanism (Mitra et al. 2018). The DNA binding constant, K_F and the number of binding sites per nucleotide, n were derived from the Scatchard equation (S10). The calculated K_F values of 1.00–22.60×10^4 M^{-1}, signify strong intercalative mode of binding. The n values which are near 1, show the presence of a single independent binding site in the CT-DNA for all the studied Pd(II) complexes. The results of the competitive fluorescence measurements are in good accord with the data obtained from the UV–Vis studies, showing that the complexes considerably interact with DNA in intercalative manner. The perturbation of the complexes on the base-stacking of CT-DNA follows the order; **Pd1 > Pd2 > Pd3 > Pd4**, consistent with the substitution kinetics trend (Table 3).
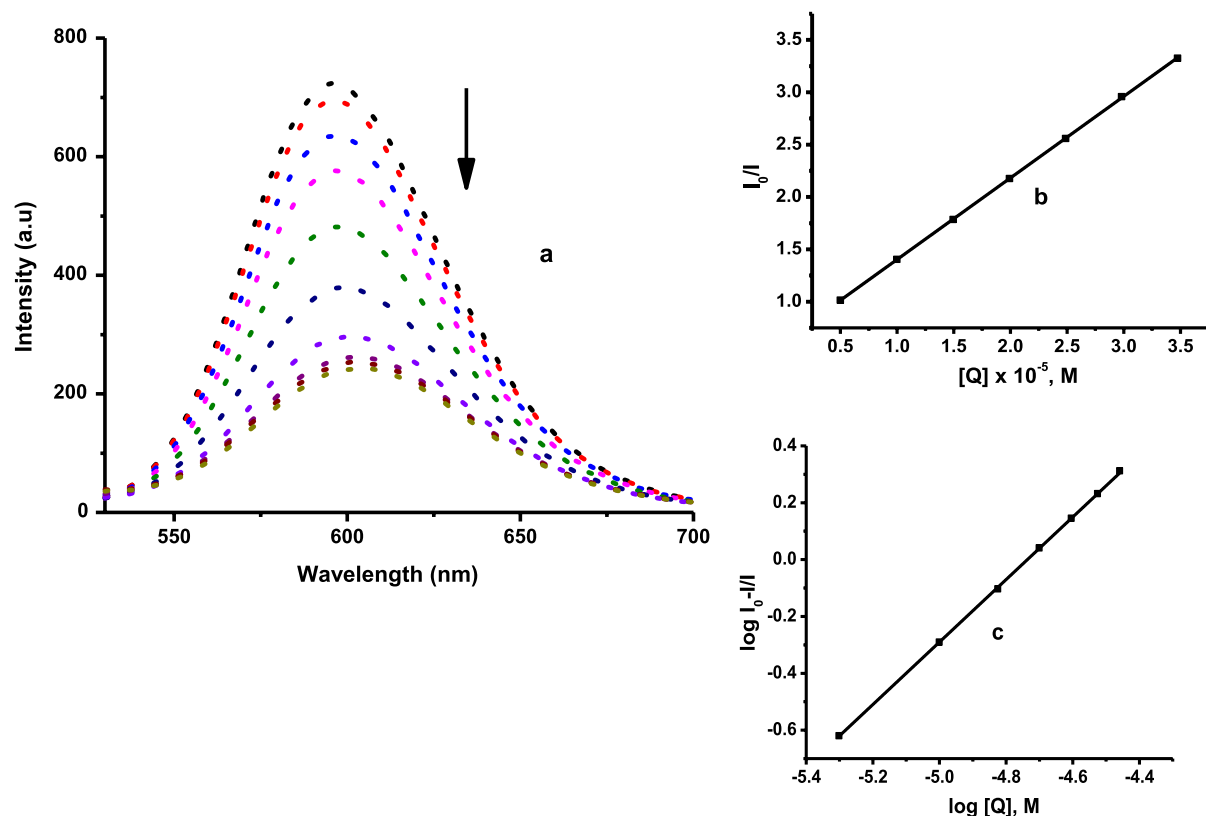
Fig. 5 a The effects of addition of **Pd1** on the emission intensity of EB bound to CT-DNA at varying concentrations. [EB]=20 µM, [CTDNA]=20 µM and [**Pd1**]=0–200 µM. The arrow shows the changes on addition of metal complex. **b** Stern–Volmer plot of I_o/I versus [Q]. **(c)** Scatchard plot of $\log[(I_o–I)/I]$ versus $\log[Q]$

Table 3 BSA binding constants and number of binding sites for the Pd(II) complexes

Complex	K_{sv} (10^5 M^{-1})	k_q (10^{13} M^{-1} s^{-1})	K_F (10^3 M^{-1})	n
Pd1	25.53 ± 0.92	11.10 ± 0.45	10.01 ± 0.38	0.77
Pd2	16.11 ± 0.90	7.01 ± 0.36	5.86 ± 0.32	0.78
Pd3	9.08 ± 0.31	3.95 ± 0.28	3.85 ± 0.30	0.84
Pd4	8.78 ± 0.33	3.82 ± 0.26	1.10 ± 0.21	0.68

BSA interactions

Fluorescence quenching measurements

Serum albumin is the most essential circulating protein in the blood plasma, among other functions it is responsible for the distribution of drugs to their pharmacological target (Elsayed et al. 2022). The fluorescence emission spectrum for **Pd1** is shown in Fig. 6, while the spectra for **Pd2**–**Pd4** are provided in Figs. S42–S44, respectively. The intensity of the characteristic broad emission band at 281 nm shows notable decreasing trends with increasing concentration of complexes **Pd1**–**Pd2** against BSA protein, suggestive of the formation of complex-BSA system. The emission intensities decrease considerably with the increasing concentration of the complexes (with no notable alteration in the emission peak position), and this could be attributed to the changes in the secondary structure of BSA causing the variation of microenvironment around BSA tryptophan (Manojkumar et al. 2019).
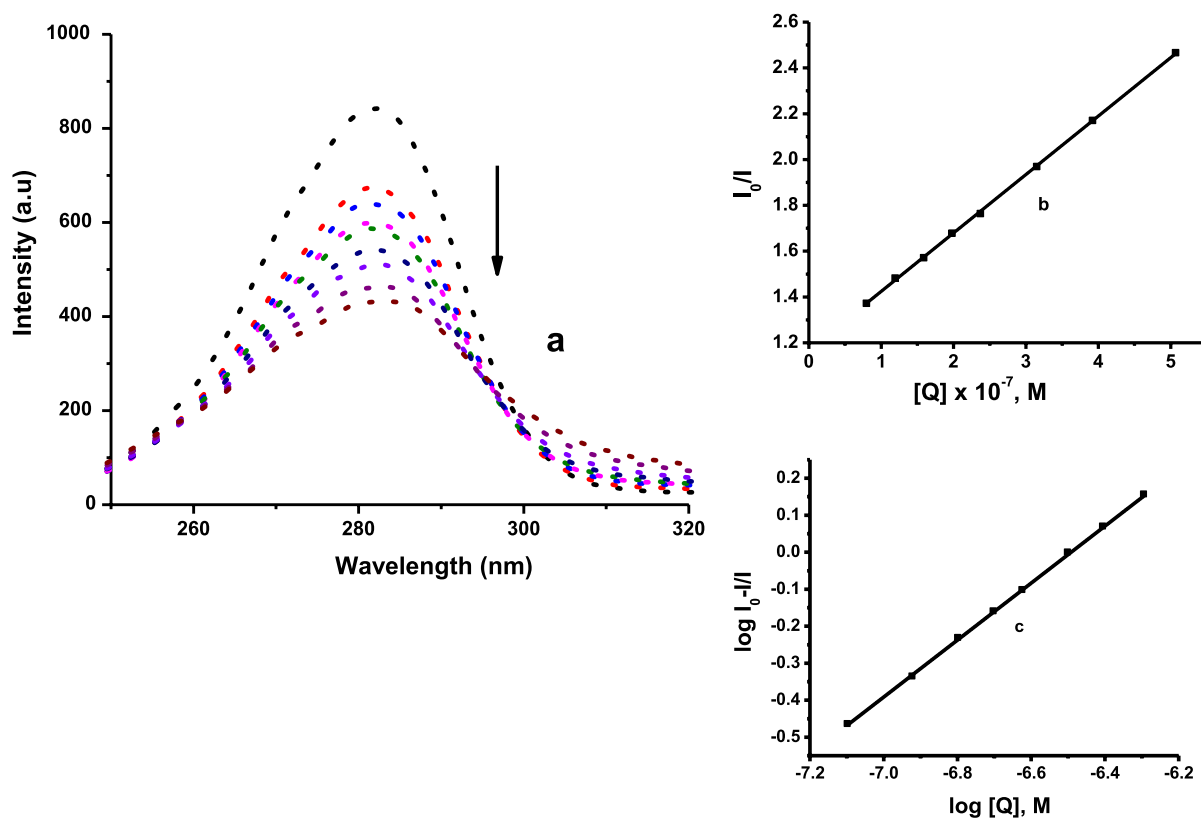
Fig. 6 a Fluorescence emission spectrum of BSA in the absence and presence of **Pd1**: [BSA]=1.2 µM and [**Pd1**]=0–200 µM. The arrow shows the changes on addition of varying quantities of **Pd1**. **b** Stern–Volmer plot of I_o/I versus [Q]. **c** Scatchard plot of log[$(I_o$–I)/I] versus log[Q]

The change in the emission intensity fitted well into the Stern–Volmer equation (K_{sv} and k_q) and Scatchard equations (K_F and n). The values of k_q, K_{SV}, K_F, and n are provided in Table 3. The values of K_{SV} (8.78–25.53×10^4 M^{-1}) illustrate that the interactions of complexes **Pd1**–**Pd4** with the protein *i.e.* BSA is not fully controlled by diffusion (Milutinović et al. 2017). Similarly, the calculated k_q values (3.82–11.10×10^{13}, M^{-1} s^{-1}), are higher than most known quenchers (10^{10} M^{-1} s^{-1}) approving static quenching mechanism (Poloni et al. 2019). Notably, the K_F values (1.10–10.01×10^3 M^{-1}) for **Pd1**–**Pd4** are within the optimum values of 10^3–10^6 M^{-1} (Topală et al. 2014), showing that the complexes can easily be transported and released to the target. The computed values of n ($\approx$ 1), reveal that only a single binding site of BSA is accessible for the interaction with the Pd(II) complexes. The BSA fluorescence quenching constants and binding constants, show strong and favourable binding of the complexes to the protein, and the order of binding is on par with the kinetic reactivity.

Molecular docking

MD simulations were performed to elucidate the binding affinities, and interactions of Pd-complexes with DNA and BSA (Figs. 7 and 8). The complexes demonstrated favourable docked score of − 6.7 kcal/mol (**Pd1**) and –6.6 kcal/mol (**Pd2**) and –6.4 kcal/mol for both **Pd3 a**nd **Pd4** (Table S11), roughly matching the experimental observations (Table 2). Docked poses and nucleotides around Pd-complexes are depicted in Figs. 7 and S44. Nucleotides DC11 & 15 and DG 16 facilitate C–H bond interactions with **Pd1**. The stability of **Pd2** is contributed significantly by π-anion and C–H bond interactions with DG12 and DA18, respectively. Additionally, the pyrazolyl

Fig. 7 The best docked
conformer of **Pd1** (**a**), **Pd2**
(**b**), **Pd3** (**c**) and **Pd4** (**d**)
with DNA duplex (scaled
ball and stick diagrams),
depicting intercalative
binding

(a)   (b)   (c)   (d)
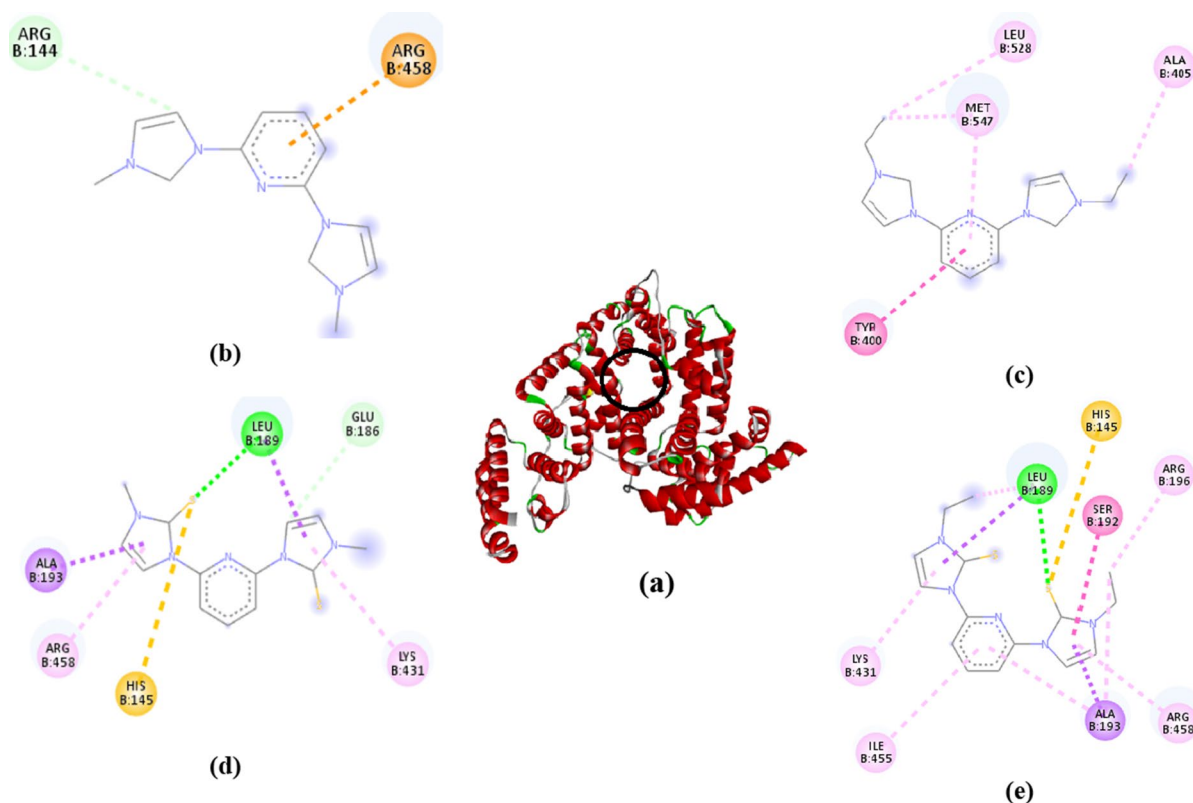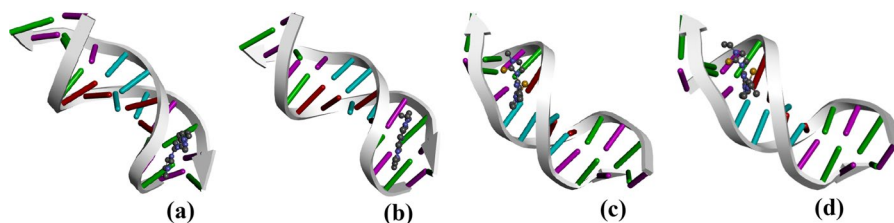

Fig. 8 **a** BSA protein binding pocket; 2D interactions of **Pd1** (**b**), **Pd2** (**c**), **Pd3** (**d**), **Pd4** (**e**) on the active site of BSA protein

moiety in both **Pd3** and **Pd4** interacts with DT 7 nucleotide through π-anion interactions. A summary of the chemical interactions of **Pd1**-**Pd4** with DNA nucleotides is provided in **Table S12**. Consistent with the experimental trend, the docked models (Fig. 7) show intercalative binding mode.

The docked BSA protein energies are ordered as **Pd1** (– 6.9 kcal/mol) > **Pd2** (– 6.5 kcal/mol) and **Pd3** (– 6.7 kcal/mol) ≈ **Pd4** (– 6.8 kcal/mol), **Table S11**, nearly agreeing with the experimental trend (Table 3). C–H bond and π-cation intermolecular interactions are formed between the pyridyl

and pyrazolyl moieties of **Pd1** with ARG144 and ARG458 amino acids, respectively. TYR400, ALA405, and LEU528 residues form π–π T-shaped and π-alkyl (MET547) interactions with **Pd2**. Also, conventional H bond (LEU189), C–H bond (GLU186), π-sulfur (HIS145), π-alkyl (LYS431, ARG458 and ILE455) and π–σ (ALA193) interactions are pre-dominant in both **Pd3** and **Pd4**. A list of intermolecular interactions together with the active amino acids of **Pd1**-**Pd4** are given in **Table S12**.

Conclusions

In summary, the syntheses and structural elucidation of Pd(II) complexes bearing CNC and SNS pincer-type ligands was achieved. The molecular structure of **Pd2** reveal a distorted square planar geometry. Kinetic reactivity of the Pd-complexes with the biological nucleophiles is controlled by both electronic and ring strain of the chelating ligands. DFT simulations of the complexes agree with the observed kinetic trends. The values of $\Delta H^{\neq}$, $\Delta S^{\neq}$ and $\Delta G^{\neq}_{25\ °C}$ reveal an associative mode of substitution reactions. Isokinetic linear relationships support a single reaction pathway. Overall spectroscopic methods indicate intercalation binding mode, and the binding order matches kinetic lability. The energy calculations of the docked models show reasonable binding affinities of the Pd-complexes to both DNA and BSA. The models also show that the complexes are tightly anchored on the active sites of DNA and protein and confirmed the intercalating binding mode observed in the experimental studies.

Supplementary data

The supplementary material contains the detailed procedures for ligand synthesis, X-ray crystallography analyses, DFT, electrochemical, stability, substitution kinetics, DNA/BSA, molecular studies, NMR, FT-IR spectroscopic spectral and mass spectral data. The material also contains DFT structures, CV voltammograms, substitution kinetics plots, UV-vis and fluorescence spectra, molecular diagrams and Tables. The crystallographic data entry for compound Pd2 is given by the deposition number CCDC 2179373.

Author contributions ROO: conceptualisation, experimental, data curation and drafting- original draft. DJ: conceptualisation, funding acquisition, supervision, writing-review, and editing of manuscript. SOO: conceptualization, funding acquisition, supervision, project administration and writing-review and editing.

Declarations

Conflict of interest The authors declare that they have no known competing financial interests or personal relationships that could have appeared to influence the reported.

References

Akkoç S, Kayser V, İlhan İÖ, Hibbs DE, Gök Y, Williams PA et al (2017) New compounds based on a benzimidazole nucleus: synthesis, characterization and cytotoxic activity against breast and colon cancer cell lines. J Organomet Chem 839:98–107

Al Nasr I, Touj N, Koko W, Khan T, Özdemir I, Yaşar S et al (2020) Biological activities of nhc–pd (Ii) complexes based on benzimidazolylidene n-heterocyclic carbene (nhc) ligands bearing aryl substituents. Catalysts 10:1190

Atwood JD (1997) Inorganic and organometallic reaction mechanisms. VCH Publishers

Balakrishnan N, Haribabu J, Krishnan DA, Swaminathan S, Mahendiran D, Bhuvanesh NS et al (2019) Zinc (II) complexes of indole thiosemicarbazones: DNA/protein binding, molecular docking and in vitro cytotoxicity studies. Polyhedron 170:188–201

Bellam R, Jaganyi D, Mambanda A, Robinson R (2018) Role of a 2, 3-bis (pyridyl) pyrazinyl chelate bridging ligand in the reactivity of Ru (ii)–Pt (ii) dinuclear complexes on the substitution of chlorides by thiourea nucleophiles—a kinetic study. New J Chem 42:12557–12569

Bellam R, Jaganyi D, Mambanda A, Robinson R, BalaKumaran MD (2019) Seven membered chelate Pt (ii) complexes with 2, 3-di (2-pyridyl) quinoxaline ligands: studies of substitution kinetics by sulfur donor nucleophiles, interactions with CT-DNA, BSA and in vitro cytotoxicity activities. RSC Adv 9:31877–31894

Bernd MA, Bauer EB, Oberkofler J, Bauer A, Reich RM, Kühn FE (2020) Macrocyclic NHC complexes of group

10 elements with enlarged aromaticity for biological studies. Dalton Trans 49:14106–14114

Chen JC, Lin IJ (2000) The first dicarbene double helical mercury complex. J Chem Soc Dalton Trans 6:839–840

Collado-Martinez A, Bohnenberger J, Oliva-Madrid M-J, Nun P, Cordes DB, Slawin AM et al (2016) Synthesis of AuI-and AuIII-Bis (NHC) complexes: ligand influence on oxidative addition to AuI species. Eur J Inorg Chem 25:4111–4122

Cooper SRI (2020) Showcasing research from Andre Frade and Richard Cooper from the Chemical Crystallography lab at the University of Oxford and Patrick McCabe at the Cambridge Crystallographic Data .Centre Increasing the performance, trustworthiness and. Cryst Eng Comm 22:7186

Cory M, McKee DD, Kagan J, Henry D, Miller JA (1985) Design, synthesis, and DNA binding properties of bifunctional intercalators. Comparison of polymethylene and diphenyl ether chains connecting phenanthridine. J Am Chem Soc 107:2528–2536

Elsayed SA, Elnabky IM, di Biase A, El-Hendawy AM (2022) New mixed ligand copper (II) hydrazone-based complexes: Synthesis, characterization, crystal structure, DNA/RNA/BSA binding, in vitro anticancer, apoptotic activity, and cell cycle analysis. Appl Organomet Chem 36:e6481

Fong TTH, Lok CN, Chung CYS, Fung YME, Chow PK, Wan PK et al (2016) Cyclometalated palladium (II) N-heterocyclic carbene complexes: anticancer agents for potent in vitro cytotoxicity and in vivo tumor growth suppression. Angew Chem Int Ed 55:11935–11939

Franich AA, Živković MD, Ćoćić D, Petrović B, Milovanović M, Arsenijević A et al (2019) New dinuclear palladium (II) complexes with benzodiazines as bridging ligands: interactions with CT-DNA and BSA, and cytotoxic activity. J Biol Inorg Chem 24:1009–1022

Ghavale N, Manjare ST, Singh HB, Butcher RJ (2015) Bis (chalcogenones) as pincer ligands: isolation and heck activity of the selone-ligated unsymmetrical C, C, Se–Pd pincer complex. Dalton Trans 44:11893–11900

Ghdhayeb MZ, Haque RA, Budagumpi S, Ahamed MBK, Majid AMA (2017) Mono-and bis-N-heterocyclic carbene silver (I) and palladium (II) complexes: Synthesis, characterization, crystal structure and in vitro anticancer studies. Polyhedron 121:222–230

Groom CR, Bruno IJ, Lightfoot MP, Ward SC (2016) The Cambridge structural database. Acta Crystallogr, Sect b: Struct Sci Cryst Eng Mater 72:171–179

Han Y-F, Zhang L, Weng L-H, Jin G-X (2014) H2-Initiated reversible switching between two-dimensional metallacycles and three-dimensional cylinders. J Am Chem Soc 136:14608–14615

Hindi KM, Panzner MJ, Tessier CA, Cannon CL, Youngs WJ (2009) The Medicinal applications of imidazolium carbene−metal complexes. Chem Rev 109:3859–3884

Hussaini SY, Haque RA, Razali MR (2019) Recent progress in silver (I)-, gold (I)/(III)-and palladium (II)-N-heterocyclic carbene complexes: a review towards biological perspectives. J Organomet Chem 882:96–111

Jia W-G, Huang Y-B, Jin G-X (2009) Synthesis, characterization of novel half-sandwich iridium and rhodium complexes containing pyridine-based organochalcogen ligands. J Organomet Chem 694:4008–4013

Jia W-G, Dai Y-C, Zhang H-N, Lu X, Sheng E-H (2015) Synthesis and characterization of gold complexes with pyridine-based SNS ligands and as homogeneous catalysts for reduction of 4-nitrophenol. RSC Adv 5:29491–29496

Jia WG, Du TT, Gao LL, Du J (2020) Synthesis, characterization, and catalytic activity of half-sandwich ruthenium complexes with pyridine/phenylene bridged NHC= E (NHC= N-heterocyclic carbene, E= S, Se) ligands. Appl Organomet Chem 34:e5651

Jomaa MY, Altaf M, Ahmad S, Alhoshani A, Baig N, Kawde A-N et al (2018) Synthesis, characterization and anticancer evaluation of transplatin derivatives with heterocyclic thiones. Polyhedron 141:360–368

Jovanović S, Obrenčević K, Bugarčić ŽD, Popović I, Žakula J, Petrović B (2016) New bimetallic palladium (II) and platinum (II) complexes: studies of the nucleophilic substitution reactions, interactions with CT-DNA, bovine serum albumin and cytotoxic activity. Dalton Trans 45:12444–12457

Karami K, Alinaghi M, Amirghofran Z, Lipkowski J (2018) Synthesis and characterization of two new trans palladium (II) complexes containing benzylamine ligand: DNA/BSA interactions, molecular docking and in vitro cytotoxic activity. Inorg Chim Acta 471:797–807

Karami K, Jamshidian N, Zakariazadeh M (2019) Synthesis, characterization and molecular docking of new C, N-palladacycles containing pyridinium-derived ligands: DNA and BSA interaction studies and evaluation as anti-tumor agents. Appl Organomet Chem 33:e4728

Koumousi ES, Zampakou M, Raptopoulou CP, Psycharis V, Beavers CM, Teat SJ et al (2012) First palladium (II) and platinum (II) complexes from employment of 2, 6-diacetylpyridine dioxime: synthesis, structural and spectroscopic characterization, and biological evaluation. Inorg Chem 51:7699–7710

Kumar A, Naaz A, Prakasham A, Gangwar MK, Butcher RJ, Panda D et al (2017) Potent anticancer activity with high selectivity of a chiral palladium N-heterocyclic carbene complex. ACS Omega 2:4632–4646

Lee J-Y, Lee J-Y, Chang Y-Y, Hu C-H, Wang NM, Lee HM (2015) palladium complexes with tridentate n-heterocyclic carbene ligands: selective "Normal" and "Abnormal" bindings and their anticancer activities. Organometallics 34:4359–4368

Manjare ST, Sharma S, Singh HB, Butcher RJ (2012) Facile synthesis of benzimidazolin-2-chalcogenones: NATURE of the carbon–chalcogen bond. J Organomet Chem 717:61–74

Manojkumar Y, Ambika S, Arulkumar R, Gowdhami B, Balaji P, Vignesh G et al (2019) Synthesis, DNA and BSA binding, in vitro anti-proliferative and in vivo anti-angiogenic properties of some cobalt (III) Schiff base complexes. New J Chem 43:11391–11407

Matta C, Gillespie R (2002) Understanding and interpreting molecular electron density distributions. J Chem Educ 79:1141–1152

Miecznikowski JR, Lo W, Lynn MA, Jain S, Keilich LC, Kloczko NF et al (2012) Syntheses, characterization, density

functional theory calculations, and activity of tridentate SNS zinc pincer complexes based on bis-imidazole or bis-triazole precursors. Inorg Chim Acta 387:25–36

Milutinović MM, Rilak A, Bratsos I, Klisurić O, Vraneš M, Gligorijević N et al (2017) New 4′-(4-chlorophenyl)-2, 2′: 6′, 2 ″-terpyridine ruthenium (II) complexes: synthesis, characterization, interaction with DNA/BSA and cytotoxicity studies. J Inorg Biochem 169:1–12

Mitra I, Mukherjee S, Misini B, Das P, Dasgupta S, Linert W et al (2018) Synthesis, biological evaluation, substitution behaviour and DFT study of Pd (II) complexes incorporating benzimidazole derivative. New J Chem 42:2574–2589

Mukherjee S, Mitra I, Fouzder C, Mukherjee S, Ghosh S, Chatterji U et al (2017) Effect of Pt (II) complexes on cancer and normal cells compared to clinically used anticancer drugs: cell cycle analysis, apoptosis and DNA/BSA binding study. J Mol Liq 247:126–140

Murray SG, Hartley FR (1981) Coordination chemistry of thioethers, selenoethers, and telluroethers in transition-metal complexes. Chem Rev 81:365–414

Onar G, Gürses C, Karataş MO, Balcıoğlu S, Akbay N, Özdemir N et al (2019) Palladium (II) and ruthenium (II) complexes of benzotriazole functionalized N-heterocyclic carbenes: Cytotoxicity, antimicrobial, and DNA interaction studies. J Organomet Chem 886:48–56

Ostrowska S, Scattolin T, Nolan SP (2021) N-Heterocyclic carbene complexes enabling the α-arylation of carbonyl compounds. Chem Commun 57:4354–4375

PetrovićBugarčićDeesIvanović-BurmazovićHeinemannPuchta BZiDAIFWR et al (2012) Role of π-acceptor effects in controlling the lability of novel monofunctional Pt (II) and Pd (II) complexes: Crystal structure of [Pt (tripyridinedimethane) Cl] Cl. Inorg Chem 51:1516–1529

Poloni DM, Dangles O, Vinson JA (2019) Binding of plant polyphenols to serum albumin and LDL: healthy implications for heart disease. J Agric Food Chem 67:9139–9147

Protas AV, Popova EA, Mikolaichuk OV, Porozov YB, Mehtiev AR, Ott I et al (2018) Synthesis, DNA and BSA binding of Pd (II) and Pt (II) complexes featuring tetrazolylacetic acids and their esters. Inorg Chim Acta 473:133–144

Rani V, Singh HB, Butcher RJ (2017) Bis (selone) complexes of palladium (II), platinum (II), and gold (III): Synthesis and structural studies. Eur J Inorg Chem 2017:3720–3728

Ray S, Mohan R, Singh JK, Samantaray MK, Shaikh MM, Panda D et al (2007) Anticancer and antimicrobial metallopharmaceutical agents based on palladium, gold, and silver N-heterocyclic carbene complexes. J Am Chem Soc 129:15042–15053

Sathyadevi P, Krishnamoorthy P, Butorac RR, Cowley AH, Bhuvanesh NS, Dharmaraj N (2011) Effect of substitution

and planarity of the ligand on DNA/BSA interaction, free radical scavenging and cytotoxicity of diamagnetic Ni (II) complexes: a systematic investigation. Dalton Trans 40:9690–9702

Seliman AA, Altaf M, Onawole AT, Ahmad S, Ahmed MY, Al-Saadi AA et al (2017) Synthesis, X-ray structures and anticancer activity of gold (I)-carbene complexes with selenones as co-ligands and their molecular docking studies with thioredoxin reductase. J Organomet Chem 848:175–183

Shabbir M, Akhter Z, Ahmad I, Ahmed S, Shafiq M, Mirza B et al (2016) Schiff base triphenylphosphine palladium (II) complexes: Synthesis, structural elucidation, electrochemical and biological evaluation. J Mol Struct 1118:250–258

Tarushi A, Lafazanis K, Kljun J, Turel I, Pantazaki AA, Psomas G et al (2013) First-and second-generation quinolone antibacterial drugs interacting with zinc (II): Structure and biological perspectives. J Inorg Biochem 121:53–65

Teyssot M-L, Jarrousse A-S, Manin M, Chevry A, Roche S, Norre F, et al. (2009) Metal-NHC complexes: a survey of anti-cancer properties. Dalton Trans 35:6894–902

Topală T, Bodoki A, Oprean L, Oprean R (2014) Bovine serum albumin interactions with metal complexes. Clujul Med 87:215

Wang Y, Robinson GH (2011) Carbene stabilization of highly reactive main-group molecules. Inorg Chem 50:12326–12337

Wei X, Yang Y, Ge J, Lin X, Liu D, Wang S et al (2020) Synthesis, characterization, DNA/BSA interactions and in vitro cytotoxicity study of palladium (II) complexes of hispolon derivatives. J Inorg Biochem 202:110857

Yang L, Powell DR, Houser RP (2007) Structural variation in copper (I) complexes with pyridylmethylamide ligands: structural analysis with a new four-coordinate geometry index, τ 4. Dalton Trans 9:955–964

Zhang L, Yan T, Han Y-F, Hahn FE, Jin G-X (2015) Synthesis of a new type of alkene metal complex using face-capping thione-alkene ligands. Dalton Trans 44:8797–8800

Zhao J, Xu Z, Lin J, Gou S (2017) Exploring the hydrolytic behavior of the platinum (IV) complexes with axial acetato ligands. Inorg Chem 56:9851–9859